A spatially-resolved large cavity of the J0337 protoplanetary disk in perseus

Uyama, T.; Ruane, G.; Lawson, K.; Muto, T.; Beichman, C.; Marel, N. van der

A Spatially-resolved Large Cavity of the J0337 Protoplanetary Disk in Perseus

Taichi Uyama[1,2,3] , Garreth Ruane[4] , Kellen Lawson[5] , Takayuki Muto[6], Charles Beichman[1,2] , and
Nienke van der Marel[7,8]

[1] Infrared Processing and Analysis Center, California Institute of Technology, 1200 E. California Boulevard, Pasadena, CA 91125, USA; tuyama@ipac.caltech.edu
[2] NASA Exoplanet Science Institute, Pasadena, CA 91125, USA
[3] National Astronomical Observatory of Japan, 2-21-1 Osawa, Mitaka, Tokyo 181-8588, Japan
[4] Jet Propulsion Laboratory, California Institute of Technology, 4800 Oak Grove Drive, Pasadena, CA 91109, USA
[5] Department of Physics and Astronomy, University of Oklahoma, Norman, OK 73019, USA
[6] Division of Liberal Arts, Kogakuin University 2665-1, Nakano-cho, Hachioji-chi, Tokyo, 192-0015, Japan
[7] Leiden Observatory, Niels Bohrweg 2, 2333 CA Leiden, The Netherlands
[8] Physics & Astronomy Department, University of Victoria, 3800 Finnerty Road, Victoria, BC, V8P 5C2, Canada

Abstract

We present Keck/NIRC2 $K_p L_p$ high-contrast imaging observations of a J0337 protoplanetary disk. The data discover the spatially-resolved large cavity, which is the second report among protoplanetary disks in the Perseus star-forming region after the LkHα 330 system. Our data and forward modeling using RADMC-3D suggests ∼80 au for the cavity radius. There is discrepancy between J0337's spectral energy distribution (SED) and the modeled SED at ∼10 μm and this suggests an unseen inner disk. We also searched for companions around J0337 but did not detect any companion candidates at separations between 0″1 and 2″5. The L_p-band detection limit corresponds to ∼20M_{Jup} at 60 au, ∼9–10M_{Jup} at 90 au, and ∼3M_{Jup} at >120 au. Compared with other young systems with large cavities such as PDS 70 and RX J1604, multiple Jovian planets, a single eccentric Jovian planet, or a massive brown dwarf at an inner separation could exist within the cavity.

Unified Astronomy Thesaurus concepts: Protoplanetary disks (1300); Planet formation (1241)

1. Introduction

Perseus is one of the nearby star-forming regions (∼300 pc derived by Gaia and VLBA observations; Ortiz-León et al. 2018) and has a young age (∼1–3 Myr for major clusters of IC 348 and NGC 1333; Luhman et al. 2016). Spectroscopic studies have reported some possible transitional disks in Perseus—for example, van der Marel et al. (2016) used Spitzer photometry and IRS data and identified several dozens of transitional disk candidates, some of which potentially have large cavities (>50 au). Transition disk cavities have been linked to both photoevaporative clearing as part of the evolutionary disk dissipation process (Alexander et al. 2014) and to the clearing by massive protoplanets which are already forming in the disk (Lin & Papaloizou 1979). Previous observational studies suggested Jovian planets in the transitional disk with cavity >50 au (e.g., RX J1604, PDS 70; Hashimoto et al. 2012; Dong et al. 2017) and eventually Very Large Telescope/SPHERE high-contrast imaging observations reported the first convincing protoplanet in the PDS 70 disk (Keppler et al. 2018). However, the number of convincing protoplanets embedded in protoplanetary disks is still small and it is important for better understandings of planet-formation mechanisms to detect/characterize more protoplanets.

2MASS J03370363+3039291 (hereafter J0337) is a member of the Perseus star-forming region, although slightly isolated from IC 348 and NGC 1333, with an IR excess. van der Marel et al. (2016) suggested a large gap in its disk from the archival Spitzer catalog. However, other than the gap information a limited number of stellar/disk parameters are known in this system because this system has not been prioritized compared with other YSOs in the major clusters. Here we present Keck/ NIRC2 high-contrast imaging observations to report that our data affirmed the large cavity as predicted in van der Marel et al. (2016). Section 2 describes our observations and data reduction. In Section 3 the result of the postprocessing is presented. Finally we present our spectral energy distribution (SED) fitting and forward modeling results and discuss the gap opening mechanisms in the J0337 disk in Section 4.

2. Observations and Data Reduction

2.1. Observations

J0337 was chosen from the sample of new transition disk candidates with large cavities from van der Marel et al. (2016), based on SED analysis of hundreds of Spitzer-selected YSOs. J0337 was selected based on its optical brightness (Principal Investigator: Nienke van der Marel). On UT 2016 October 15 we observed J0337 by Keck/NIRC2 L_p band (3.776 μm) combined with the vector vortex mask and with the total exposure time of 2120 s, providing the parallactic angle change of 91°33. After confirming the disk feature (see Section 3) we conducted follow-up observations for this target using NIRC2 K_p band (2.124 μm) on UT 2021 February 2 without a coronagraph mask (Principal Investigator: Garreth Ruane; backup target). We achieved 2100 s and 38°94 for the total exposure time and the parallactic angle change. Both observations were conducted under the vertical angle mode for angular differential imaging (ADI; Marois et al. 2006) to suppress the stellar halo and instrumental speckles. The typical full-width at half maximum (FWHM) of the point-spread function (PSF) measured 9 pix (∼90 mas) at L_p band and 5 pix (∼50 mas) at K_p band, respectively. We note that no reference-PSF stars for reference-star differential imaging (RDI; e.g., Ruane et al.
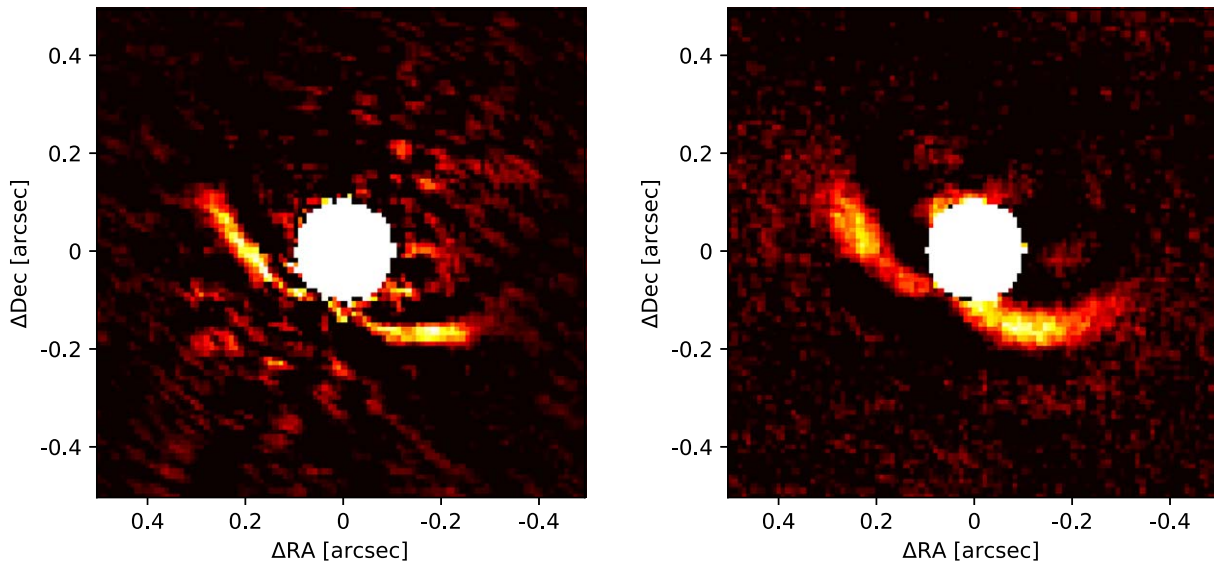
Figure 1. Keck/NIRC2 observations of J0337 at K_p band (left) and L_p band (right). KL = 4 is adopted for both images. The central star is masked by the algorithms. North is up and east is left.

2019) were observed in both epochs and we apply only ADI for postprocessing.

2.2. Data Reduction

First we preprocessed (bad pixel correction, flat-fielding, sky subtraction, and image registration) the obtained NIRC2 raw frames (see also Ruane et al. 2019). We then performed ADI-based postprocessing to subtract the stellar halo by producing the most likely reference PSFs combined with the `pyKLIP` algorithms[9] (Wang et al. 2015) that utilized Karhunen–Loève Image Projection (KLIP; Soummer et al. 2012). We adopted minrot = 10° in the `pyklip` setting, which is not the most aggressive parameters for the ADI reduction, so that we can avoid a severe self-subtraction effect that distorts the geometry and attenuates the flux of the disk features within $\rho \leqslant 0\rlap{.}''3$ detected in our observations (see Section 3 for the ADI results).

3. Results

In both epochs we confirmed the same arc-like feature (see Figure 1) with a signal-to-noise ratio (S/N) ~ 4–5 for its spine, which indicates that the arc feature is gravitationally bound to J0337. This arc feature is likely to correspond to forward-scattered light from an inner edge of the outer disk around J0337. The backward-scatter components are not detected in our observations. Considering the S/N and the aggressiveness for the ADI reduction to avoid severe self-subtraction that attenuates the disk feature, we adopted KL = 4 to present our results. However, note that this nonaggressive postprocessing still leaves self-subtraction. We conducted injection test by burying artificial point sources at a variety of separations and position angles, which resulted in >50% self-subtraction particularly in the K_p-band data occurs within $0\rlap{.}''3$ because of its small field rotation angle. The inner dark region indicates a cavity of $\sim 0\rlap{.}''25$ in radius, which is consistent with the prediction from the SED fitting study ($r_{in} = 50^{+30}_{-10}$ au; van der Marel et al. 2016). From the geometry of the arc feature we roughly estimate an inclination and a position angle to be $\sim 60°$

and $\sim 25°$, respectively. The gap size is estimated by forward modeling (see Section 4.2). Our high-contrast imaging results show the second large cavity in the Perseus transitional disks after the LkHα 330 system where a large cavity and a pair of spirals were reported in its disk (Isella et al. 2013; Akiyama et al. 2016; Uyama et al. 2018).

4. Discussions

4.1. SED Fitting for Stellar Parameters

Due to a lack of known spectral type, van der Marel et al. (2016) adopted $A_v = 0.0$ but the Bayester19 dust map (Green et al. 2019) suggests $A_v \sim 1.4$ mag around J0337, thus we corrected the photometry data from published survey data between UV and near-IR wavelengths. Figure 2 shows J0337's SED ranging between UV and sub-mm wavelengths (see also Appendix A), and we note that the previous surveys detected no flux at wavelengths longer than 200 μm. For SED fitting, we permitted A_v values in the range 1.38–1.46 (the 1σ range about the nominal value from the Bayestar19 dust map). Note that we do not account for circumstellar materials such as envelopes, if any, and in this sense the effective extinction may be underestimated. We used available GALEX (Martin et al. 2005), TYCHO (Høg et al. 2000), Gaia (Gaia Collaboration et al. 2016), SDSS (Blanton et al. 2017), APASS (Henden & Munari 2014), and 2MASS (Skrutskie et al. 2006) JH-band data points for the stellar characterizations (the best-fit parameters: $T_{eff} \sim 7800$ K, $\log g \sim 5.0$, $L_\star \sim 9.3 L_\odot$, and $M_\star \sim 1.4 M_\odot$ for $A_v = 1.38$). SED retrieval, dereddening, and fitting were carried out using the Virtual Observatory SED Analyzer (VOSA; Bayo et al. 2008). For SED fitting, we utilized the BT-Settl-AGSS2009 synthetic stellar spectra (Asplund et al. 2009; Allard et al. 2012). The VOSA "Chi-square Fit" tool was used to determine the best-fit parameter values provided above. However, results from other VOSA SED fitting routines provide comparable solutions (e.g., the "Model Bayes Analysis" indicates a 1σ confidence interval for T_{eff} in the range 7444–7800 K). For comparison, we also performed fitting for $A_v = 0$ (no extinction; van der Marel et al. 2016); in either case, the derived best-fit parameters are well located in the 1–5 Myr range of the MIST evolutionary models (see the left panel of Figure 2; for details see
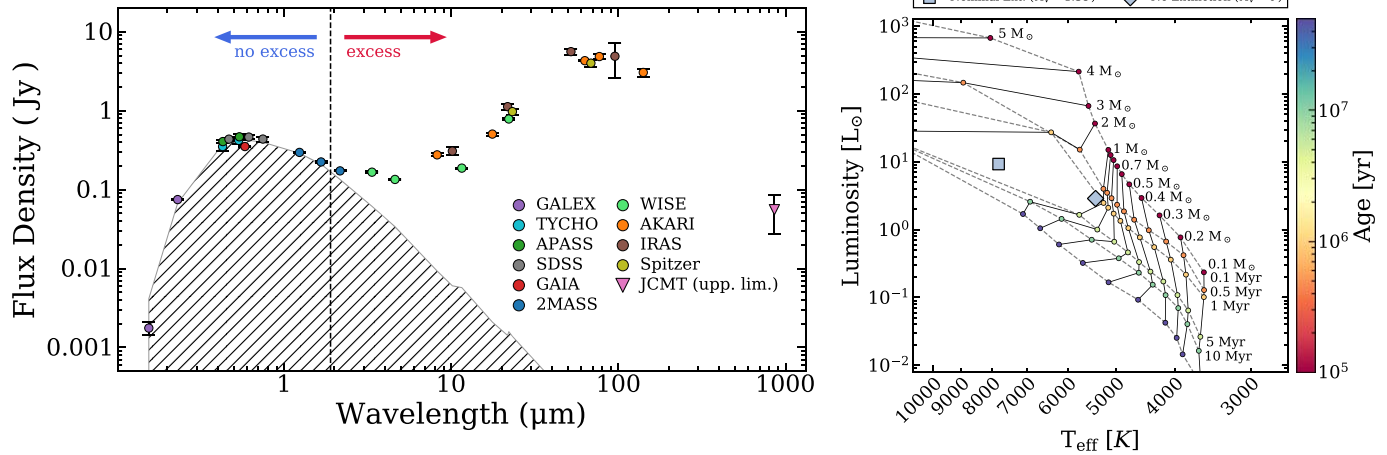

Figure 2. (Left) SED of J0337 overlaid with the best-fit stellar photosphere indicated by the gray hatched region. We used only the data points to the left of the vertical dashed line to characterize the stellar parameters. The points to the right of the vertical dashed line are regarded as the IR excess, the disk parameters for which are estimated in van der Marel et al. (2016). The inverted triangular point indicates an upper limit. The archival photometry is summarized in Appendix A. (Right) Comparison of MIST evolutionary tracks (solid lines) and isochrones (dashed lines) with the best-fit parameters of J0337's SED, assuming either the nominal A_V value or no extinction. These parameters are consistent with a 1–5 Myr star, in agreement with the age estimate of the Perseus star-forming region.

Dotter 2016). For further characterizations of the stellar parameters such as accretion high-dispersion spectroscopy is helpful (Manara et al. 2014; Alcalá et al. 2017).

We also extrapolated the disk parameters using the updated Gaia-based distance of 303 pc (Gaia Collaboration et al. 2018). As mentioned in van der Marel et al. (2016) the estimated disk mass has large uncertainty because the SED fitting at wavelengths shorter than millimeter can trace only optically thick part of the disk. We use an upper limit of the JCMT/SCUBA-2 850 μm observations, which is converted into $< 20 M_{\rm Jup}$ with Equation (5) in van der Marel et al. (2016), for the discussion of the disk evolution mechanism. In Section 4.2 we also discuss the radiative transfer modeling to reproduce the outer arc feature. However, we applied ADI technique to remove stellar halo and to detect the disk scattered light, which attenuates and distorts the disk feature. Therefore in this study we focus on the detection of the spatially-resolved large cavity. The detailed modeling will be performed with the follow-up polarimetric differential imaging (PDI; Kuhn et al. 2001) or RDI data as well as (sub)millimeter observations of the J0337 disk.

4.2. Forward Modeling

To validate the cavity size, we forward modeled the disk feature to the NIRC2 data using RADMC-3D radiative transfer code (Dullemond et al. 2012) and `pyklip` forward modeling modules. As mentioned in Section 4.1, however, it is difficult to estimate the detailed disk parameters with the current SED data points and we aim at reproducing the NIRC2 image and the MIR excess of the SED in the forward modeling processes. For simplicity we fix the inclination $= 60°$ and position angle $= -25°$ in the modeling. We found that the inner wall of the outer disk needs to have low surface density so that the forward scattering is brighter than the backward scattering with inclination $\sim 60°$, which can reproduce the NIRC2 results, on the other hand the outer disk needs to have a high enough dust mass (high surface density) to reproduce the MIR excess. A power-law density profile ($\Sigma_{\rm dust} \propto r^{-0.5}$, where $\Sigma_{\rm dust}$ and r correspond to the dust surface density and separation from the star, respectively) can reproduce either of these two characteristics but cannot reproduce both simultaneously. Therefore, for

reproducing both characteristics we utilized a Gaussian profile

$$\Sigma_{\rm dust}(r) = \Sigma_{\rm center} * \exp(-(r - r_{\rm center})^2 / 2\sigma_r^2), \quad (1)$$

where $\Sigma_{\rm center} = 5 \times 10^{-3}$ g cm^{-2}, $r_{\rm center} = 200$ au, and $\sigma_r = 50$ au (note that these parameters are degenerate). In this paper, we fix $\Sigma_{\rm center}$, $r_{\rm center}$, and σ_r since near-IR does not in general trace dust surface density. The dust surface density distribution will be better constrained by spatially-resolved sub-mm observations with e.g., ALMA.

We also adopted a dust settling factor $f_{\rm set} = 2$ to match the observational results and a scale height is calculated as $\frac{\sqrt{kT_{\rm dust}/(2.34m_{\rm H})}}{f_{\rm set}\sqrt{GM_\star/r^3}}$, where k, $T_{\rm dust}$, $m_{\rm H}$, and G are the Boltzmann constant, dust temperature, mass of hydrogen, and gravitational constant, respectively. We used thermal Monte Carlo computations of RADMC-3D (mctherm) to calculate the dust temperature derived from the adopted dust density profile and the stellar parameters. We then utilized the Mie scattering codes (Bohren & Huffman 1983) with the Gaussian dust-size distribution (centered around 10 μm, 5% width) and the optical constant of amorphous silicate[10] to calculate dust opacity. These assumptions provide a good match to the catalog values around MIR and we tested the cavity size by defining a cutoff of the modeled disk ($\Sigma_{\rm dust}(r) = 0$ at $r < r_{\rm cutoff}$ in Equation (1)) as the cavity radius and changing it from 40 au to 100 au by a 20 au step. We injected the modeled disk to the NIRC2 data at a position angle of $-115°$ (rotated by 90° clockwise) and then rereduced them. The 80 au cavity model seems to best match the NIRC2 results while the SEDs are not largely affected within the parameter range of the cavity radius we explored (see Figures 3 and 4 and Appendix B). Note that because of the imperfect AO correction and the presence of the actual disk feature, the injected disk feature is affected to some extent in the postprocessed image. The $L_{\rm p}$-band forward-modeled images are less clear than the $K_{\rm p}$-band images as the $L_{\rm p}$-band observations have the larger PSF (see also Section 2.1). Particularly the southern part of the injected disk is attenuated by self-subtraction of the actual disk features. In Table 1 we

---
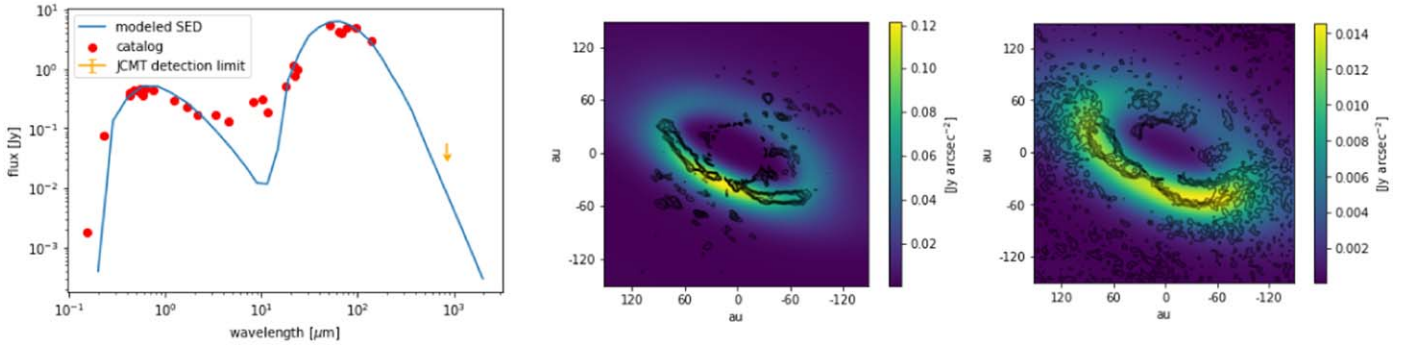
[10] http://www.astro.uni-jena.de/Laboratory/OCDB/data/silicate/amorph/pyrmg70.lnk

Figure 3. The adopted model assuming the cavity size of 80 au. (Left) The modeled SED in this study compared with the catalog values—we include only the stellar component with $T_{\rm eff} = 7800$ K blackbody and the outer disk component (see text). The discrepancy at $\sim$10 μm suggests an unseen inner disk. (Middle) The modeled disk image at $K_{\rm p}$ band overlaid with the NIRC2 contours. (Right) Same as the middle panel for $L_{\rm p}$ band. Note that the modeled disk images are smoothed by Gaussian with the measured FWHM of each NIRC2 observation.
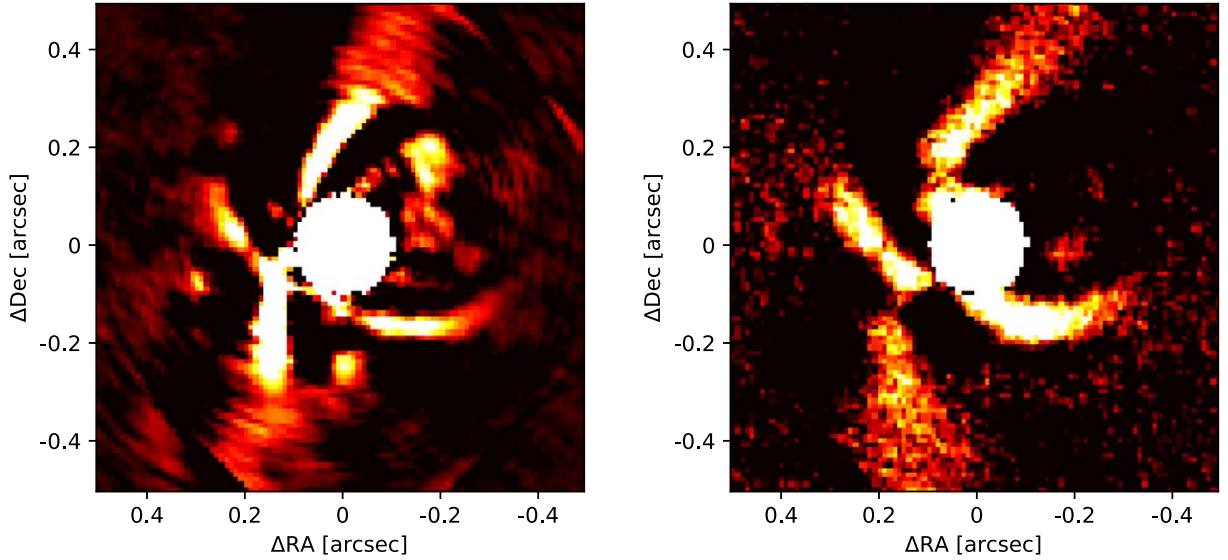

Figure 4. Postprocessed images at $K_{\rm p}$ (left) and $L_{\rm p}$ band (right) after injecting the 80 au cavity model (Figure 3) at position angle of $-115°$.

summarize the stellar and disk parameters we adopted in this study. Since the system is yet relatively unexplored and we only have images in near-IR wavelengths, it is hard determine all the model parameters. We therefore address the uncertainties of the model parameters briefly by changing stellar luminosity, whose uncertainty is expected to be a factor of a few due to the uncertainty of extinction toward the star. The change of the stellar luminosity affects the disk temperature. As shown in Appendix C, we see that the modeled SED is affected by the stellar luminosity while the geometry of the modeled near-IR image is not. Therefore, we consider that the cavity radius of $\sim$80 au is relatively robust despite the uncertainty of stellar luminosity.

We also note that our modeled SED cannot reproduce the $\sim$10 μm excess and the discrepancy indicates presence of an unseen inner disk. As the NIRC2 data did not confirm any inner disk features the inner disk may be located within or close to the inner working angle of the NIRC2 observations ($\sim$0″1 = 30 au), which is indeed well outside the typical radii of inner disks (Francis & van der Marel 2020). Future interferometric observations or follow-up PDI/RDI observations will be able to discuss the inner disk. Particularly the follow-up PDI/RDI may detect a shadowing effect by the inner disk (e.g., Bohn et al. 2022) and this should be taken into account for a better model of the J0337 disk.

Table 1
Summary of the Adopted Parameters

Parameter	Value
Stellar parameters	
$T_{\rm eff}$	7800 K
log g	5.0
$L_\star$	9.3 $L_\odot$
$M_\star$	1.4 $M_\odot$
age	1–5 Myr
$A_{\rm V}$	1.38
Disk parameters	
Inclination	60°
Position angle	$-25°$
Dust distribution	Gaussian profile (Equation (1))
Cavity radius	80 au

4.3. Gap Opening Mechanism

Alexander et al. (2006) simulated the disk evolution with photoevaporation and predicted that the disk with a photoevaporation-induced cavity has the order of $M_{\rm disk} \sim 10^{-4}\ M_\star$. With the updated stellar parameters and the upper limit of the disk mass (see Section 4.1), the disk mass is $<1.4 \times 10^{-2}\ M_\star$.
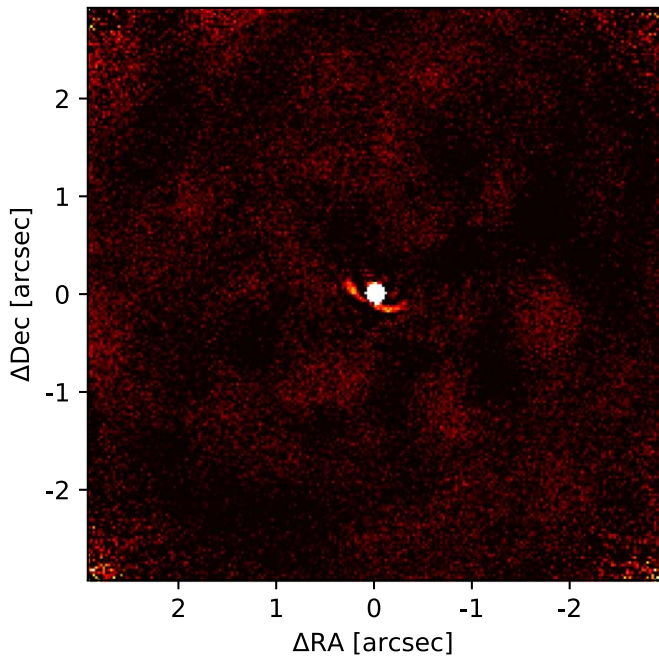
Figure 5. Same NIRC2 L_p-band result (see Figure 1) with the larger FoV and $KL = 10$ to search for outer companion candidates.

Figure 6. 5σ detection limit of the L_p-band observations made from the $KL = 10$ result (see Figure 5).

If the actual disk mass is smaller than the upper limit by an order of magnitude photoevaporation can be responsible for the cavity; but it is unlikely that photoevaporation is the only mechanism that opens such a large cavity (e.g., Espaillat et al. 2010). Accretion rate is another index to discuss the mass-loss ratio by photoevaporation (e.g., Owen et al. 2012; Ercolano & Pascucci 2017), but J0337's accretion has not been studied. Deep radio-wavelength explorations and high-dispersion spectroscopy for this system will help to determine the disk mass and to further investigate the photoevaporation scenario.

Planet formation is also one of the most plausible scenarios given that the cavity size is similar to the PDS 70 system (Keppler et al. 2018). However, our observations did not detect any convincing companion candidates at separations between 0″1 and 2″5. Figure 5 shows the L_p-band ADI result with $KL = 10$ to search for companions. Figure 6 shows 5σ detection limit of Figure 5 with the expected contrast of a substellar-mass object assuming 1 Myr and COND03 model (Baraffe et al. 2003). We divided the FoV into a number of annular regions and defined the noise as the standard deviation within each annular region, where we masked the disk feature and used 5σ clipping to mitigate the effect of the disk feature on the detection limit. We also corrected the self-subtraction effect by injecting fake sources at different position angle and separations and calculating the flux-attenuation ratio. Our detection limits could constrain the presence of a massive brown-dwarf companion in the cavity region ($\sim 20 M_{Jup}$ at 60 au and ~ 9–$10 M_{Jup}$ at 90 au) and that of a $\sim 3 M_{Jup}$ protoplanet outside the cavity (>120 au). Compared with other high-contrast imaging and simulation studies that targeted large-cavity transitional disks such as PDS 70 or RX J1604 (Canovas et al. 2017; Haffert et al. 2019; Muley et al. 2019) there could be multiple Jovian planets less than $10 M_{Jup}$, a single eccentric Jovian planet, or a brown-dwarf companion close to the central star that we cannot resolve in our observations.
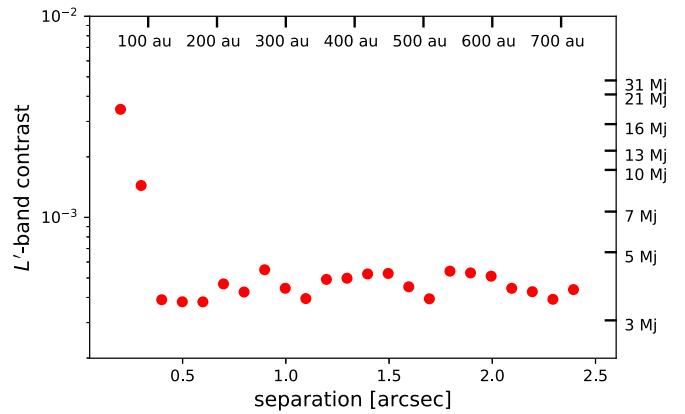
5. Summary

YSOs in Perseus are typically more distant than other nearby star-forming regions such as Taurus, Lupus, and Ophiuchus. Furthermore Perseus is located at northern in the celestial field and Perseus has been less prioritized by ALMA or adaptive optics observations. In this study we presented Keck/NIRC2 $K_p L_p$ high-contrast imaging observations of the J0337 protoplanetary disk, one of the transitional disk candidates with a large cavity suggested in van der Marel et al. (2016). After ADI reduction with `pyklip` we detected forward scattering from an inner wall of the outer disk and affirmed the large cavity. As the ADI reduction distorts the geometry of the disk, we investigated the cavity size with forward-modeled disks that are made from RADMC-3D radiative transfer codes as well as aiming to reproduce its SED. Our data and forward modeling suggest ~ 80 au for the cavity radius, which is consistent with the prediction of van der Marel et al. (2016). However there is discrepancy at $\sim 10\ \mu$m in J0337's SED and the modeled SED suggesting the presence of an unseen inner disk. We also searched for companions around J0337 but did not detect any convincing companions within 2″5 and the L_p-band detection limit could set a constraint on the mass of potential companions to $\sim 20 M_{Jup}$ at 60 au, ~ 9–$10 M_{Jup}$ at 90 au, and $\sim 3 M_{Jup}$ at >120 au assuming 1 Myr and COND03 model. Compared with other protoplanetary disk systems with large cavities such as PDS 70 and RX J1604, a massive brown-dwarf companion at an inner separation or multiple Jovian planets fainter than our detection limit within the cavity may exist inside the cavity.

The detailed modeling, including the inner disk component, will help better understand the J0337 system; while follow-up observations, such as spectroscopic observation of J0337 for the stellar characterization, PDI/RDI, to investigate the scattered light without self-subtraction, obtaining radio flux and ALMA high-angular resolution observation, are essential. Finally our discovery is the second spatially-resolved cavity in the Perseus protoplanetary disks and there remain more transitional disks suggested in SED-based studies such as van der Marel et al. (2016), which promotes further high-angular resolution observations at this region.

Appendix A
J0337 SED

Table 2 summarizes archival photometry of J0337 (see also Figure 2). Note that the photometric values in Table 2 are de-reddened in the VOSA calculations from the catalog values (see Fitzpatrick 1999 and Indebetouw et al. 2005 for the extinction law). We used those no longer than 1.7 μm for the SED fitting to estimate the stellar parameters and referred to the MIR photometry for the forward modeling.

Table 2
Archival Photometry of J0337

Wavelength (μm)	Flux (erg s^{-1} cm^{-2} μm^{-1})	Flux Error (erg s^{-1} cm^{-2} μm^{-1})	Remarks
0.155	2.2e-10	3.97e-11	GALEX (Martin et al. 2005)
0.23	4.23e-09	6.46e-11	GALEX (Martin et al. 2005)
0.428	5.75e-09	6.63e-10	TYCHO (Høg et al. 2000)
0.43	6.60e-09	2.61e-10	APASS (Henden & Munari 2014)
0.467	6.00e-09	2.65e-10	SDSS (Blanton et al. 2017)
0.534	4.43e-09	4.24e-10	TYCHO (Høg et al. 2000)
0.539	4.82e-09	4.22e-10	APASS (Henden & Munari 2014)
0.582	3.11e-09	8.17e-12	Gaia (Gaia Collaboration et al. 2016; Gaia Collaboration 2020)
0.614	3.69e-09	1.87e-10	SDSS (Blanton et al. 2017)
0.746	2.36e-09	1.67e-10	SDSS (Blanton et al. 2017)
1.235	5.83e-10	1.23e-11	2MASS (Skrutskie et al. 2006, 2019)
1.662	2.44e-10	4.71e-12	2MASS (Skrutskie et al. 2006, 2019)
2.159	1.11e-10	1.74e-12	2MASS (Skrutskie et al. 2006, 2019)
3.353	4.44e-11	9.41e-13	WISE (Wright et al. 2010, 2019)
4.603	1.91e-11	3.51e-13	WISE (Wright et al. 2010, 2019)
8.228	1.22e-11	5.39e-13	AKARI (Ishihara et al. 2010)
10.146	8.98e-12	1.08e-12	IRAS (Neugebauer et al. 1984, 2019)
11.561	4.21e-12	6.2e-14	WISE (Wright et al. 2010, 2019)
17.609	4.89e-12	2.26e-13	AKARI (Ishihara et al. 2010)
21.727	7.16e-12	5.85e-13	IRAS (Neugebauer et al. 1984, 2019)
22.088	4.83e-12	1.11e-13	WISE (Wright et al. 2010, 2019)
23.21	5.42e-12	5.04e-13	Spitzer (Evans et al. 2003; Capak 2019)
51.989	6.22e-12	5.24e-13	IRAS (Neugebauer et al. 1984, 2019)
62.951	3.26e-12	3.6e-14	AKARI (Ishihara et al. 2010)
68.445	2.57e-12	2.48e-13	Spitzer (Evans et al. 2003; Capak 2019)
76.904	2.46e-12	1.62e-13	AKARI (Ishihara et al. 2010)
95.297	1.62e-12	7.56e-13	IRAS (Neugebauer et al. 1984, 2019)
140.856	4.62e-13	5.26e-14	AKARI (Ishihara et al. 2010)
857.914	2.27e-16	1.17e-16	JCMT upper limit (van der Marel et al. 2016)

Appendix B
Forward Modeling with Different Cavity Sizes

Figures 7–9 compare the model images and the forward-modeled results assuming 40, 60, and 100 au for the cavity size (defined as a cutoff in the model) in the radius. The Gaussian radial profile for the outer disk is fixed in the modeling. Regarding the scattering profile we multiplied the K_p and L_p modeled disks by 0.8 and 2 to correct the difference between the simulated blackbody with $T_{eff} = 7800$ K and the catalog values. Considering the geometry of the disk scattered light, the 80 au cavity model best matches the NIRC2 results. In the K_p-band forward-modeled images, the 40 au and 60 au cavity models are reproduced as an almost straight line because the ADI reduction distorted the modeled disk, while the NIRC2 data show the arc feature as presented in Section 3. The 100 au cavity model shows the larger ring feature than the NIRC2 data and suggests the bright backward-scattering feature that is not seen in fact.
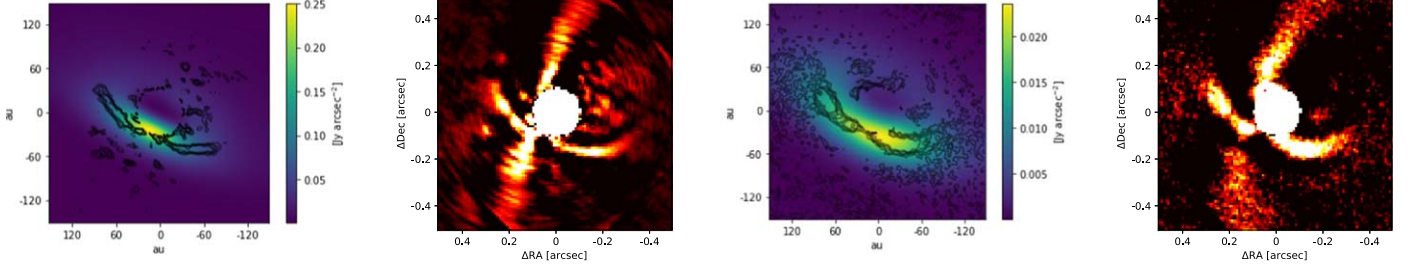

Figure 7. The modeled disk images assuming the cavity size of 40 au. From left to right: modeled disk at K_p band overlaid with the NIRC2 result contours (black), postprocessed NIRC2 image at K_p band after injecting the modeled disk (forward-modeled result), modeled disk at L_p band, and the forward-modeled result at the L_p band.
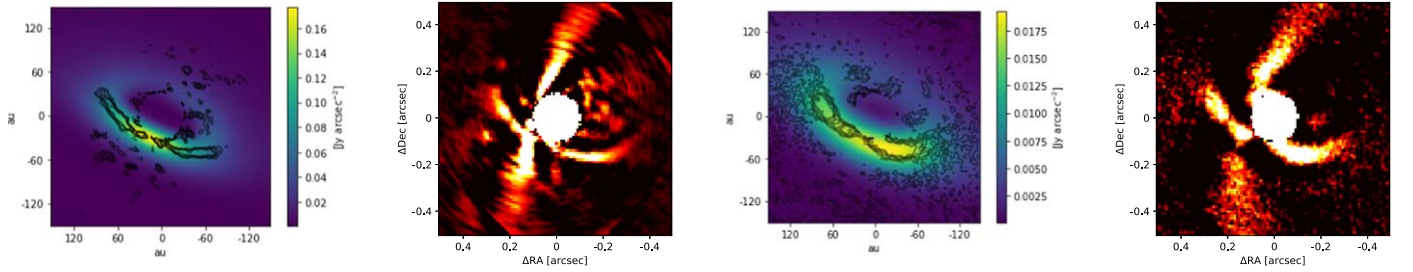

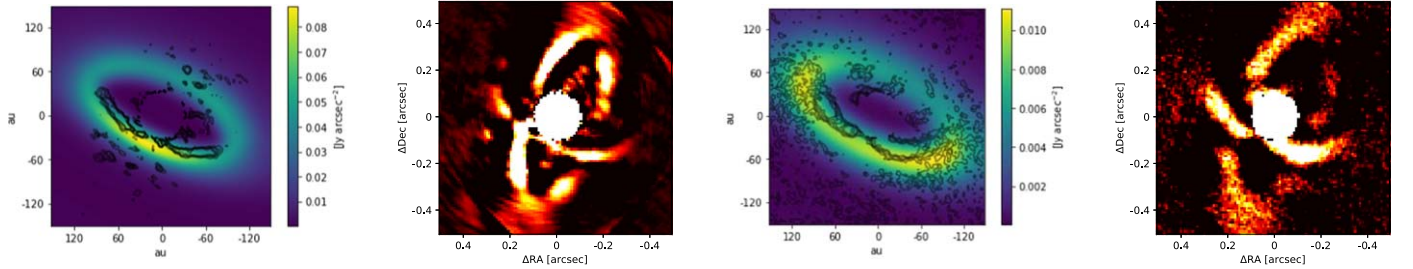**Figure 8.** Same as Figure 7 for the case of 60 au cavity.

Figure 9. Same as Figures 7 and 8 for the case of 100 au cavity.

Appendix C
RADMC-3D Modeling with Different Dust Temperatures

The uncertainty on luminosity from the VOSA fitting is 0.18 but as mentioned in Section 4.1 the uncertainty on the extinction estimation could affect characterizing the stellar parameters. To test the effect of the dust temperature on the RADMC-3D modeling results, we varied a larger range of the stellar luminosity from $3.1\,L_\odot$ ($L_\star/3$) to $27.9\,L_\odot$ ($3L_\star$) by changing the stellar temperature in the RADMC-3D settings from 5927 ($7800/3^{0.25}$) K to 10,265 ($7800 \times 3^{0.25}$) K while we fixed the cavity size to 80 au. The dust temperature was accordingly calculated by the "mctherm" command in RADMC-3D. Figure 10 shows the modeled SEDs and Figure 11 compares the modeled images with the above assumptions. The SED and surface brightness of the disk are variable with the stellar luminosity while the geometry of the disk feature does not vary within this luminosity range.
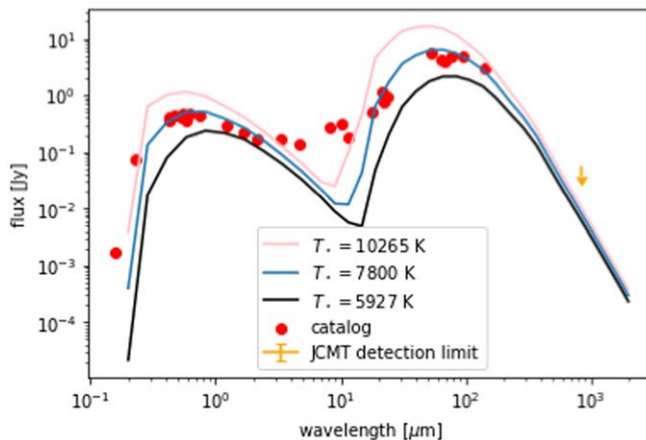

Figure 10. Comparison of the modeled SEDs assuming different temperature of the central star and the 80 au cavity. The SED with $T_\star = 7800$ K is the same as Figure 3.
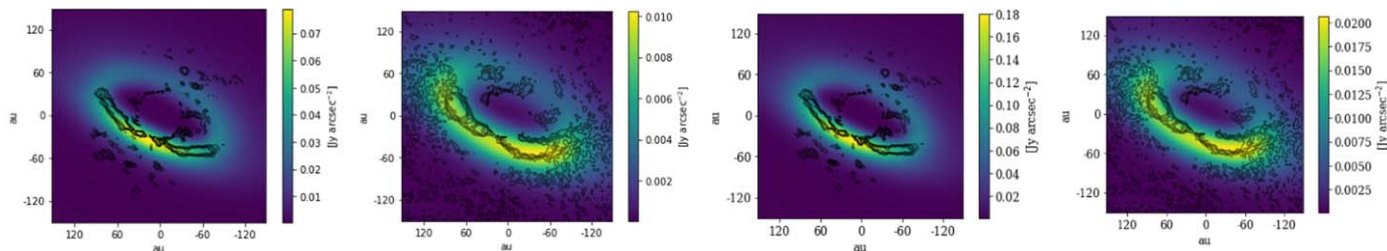

Figure 11. Comparison of the modeled images assuming different temperature of the central star and the 80 au cavity. From left to right: modeled disk at K_p band with $T_\star = 5926$ K, modeled disk at L_p band with $T_\star = 5926$, and modeled disk at K_p and L_p bands with $T_\star = 10,265$ K.

ORCID iDs

Taichi Uyama ⓘ https://orcid.org/0000-0002-6879-3030
Garreth Ruane ⓘ https://orcid.org/0000-0003-4769-1665
Kellen Lawson ⓘ https://orcid.org/0000-0002-6964-8732
Charles Beichman ⓘ https://orcid.org/0000-0002-5627-5471
Nienke van der Marel ⓘ https://orcid.org/0000-0003-2458-9756

References

Akiyama, E., Hashimoto, J., Liu, H. B., et al. 2016, AJ, 152, 222
Alcalá, J. M., Manara, C. F., Natta, A., et al. 2017, A&A, 600, A20
Alexander, R., Pascucci, I., Andrews, S., Armitage, P., & Cieza, L. 2014, Protostars and Planets VI (Tucson, AZ: Univ. of Arizona Press), 475
Alexander, R. D., Clarke, C. J., & Pringle, J. E. 2006, MNRAS, 369, 229
Allard, F., Homeier, D., & Freytag, B. 2012, RSPTA, 370, 2765
Asplund, M., Grevesse, N., Sauval, A. J., & Scott, P. 2009, ARA&A, 47, 481
Baraffe, I., Chabrier, G., Barman, T. S., Allard, F., & Hauschildt, P. H. 2003, A&A, 402, 701
Bayo, A., Rodrigo, C., Barrado Y Navascués, D., et al. 2008, A&A, 492, 277
Blanton, M. R., Bershady, M. A., Abolfathi, B., et al. 2017, AJ, 154, 28
Bohn, A. J., Benisty, M., Perraut, K., et al. 2022, A&A, 658, A183
Bohren, C. F., & Huffman, D. R. 1983, Absorption and Scattering of Light by Small Particles (New York: Wiley)
Canovas, H., Hardy, A., Zurlo, A., et al. 2017, A&A, 598, A43
Capak, P. 2019, Spitzer Enhanced Imaging Products (SEIP) Source List, IPAC, doi:10.26131/IRSA3
Dong, R., van der Marel, N., Hashimoto, J., et al. 2017, ApJ, 836, 201
Dotter, A. 2016, ApJS, 222, 8
Dullemond, C. P., Juhasz, A., Pohl, A., et al. 2012, RADMC-3D: A Multi-purpose Radiative Transfer Tool, Astrophysics Source Code Library, ascl:1202.015
Ercolano, B., & Pascucci, I. 2017, RSOS, 4, 170114
Espaillat, C., D'Alessio, P., Hernández, J., et al. 2010, ApJ, 717, 441
Evans, N. J. I., Allen, L. E., Allen, L. E., et al. 2003, PASP, 115, 965
Fitzpatrick, E. L. 1999, PASP, 111, 63
Francis, L., & van der Marel, N. 2020, ApJ, 892, 111
Gaia Collaboration 2020, Gaia Source Catalogue DR2, IPAC, doi:10.26131/IRSA12
Gaia Collaboration, Brown, A. G. A., Vallenari, A., et al. 2018, A&A, 616, A1
Gaia Collaboration, Prusti, T., de Bruijne, J. H. J., et al. 2016, A&A, 595, A1
Green, G. M., Schlafly, E., Zucker, C., Speagle, J. S., & Finkbeiner, D. 2019, ApJ, 887, 93
Haffert, S. Y., Bohn, A. J., de Boer, J., et al. 2019, NatAs, 3, 749
Hashimoto, J., Dong, R., Kudo, T., et al. 2012, ApJL, 758, L19
Henden, A., & Munari, U. 2014, CoSka, 43, 518
Høg, E., Fabricius, C., Makarov, V. V., et al. 2000, A&A, 355, L27
Indebetouw, R., Mathis, J. S., Babler, B. L., et al. 2005, ApJ, 619, 931
Isella, A., Pérez, L. M., Carpenter, J. M., et al. 2013, ApJ, 775, 30
Ishihara, D., Onaka, T., Kataza, H., et al. 2010, A&A, 514, A1
Keppler, M., Benisty, M., Müller, A., et al. 2018, A&A, 617, A44
Kuhn, J. R., Potter, D., & Parise, B. 2001, ApJL, 553, L189
Lin, D. N. C., & Papaloizou, J. 1979, MNRAS, 188, 191
Luhman, K. L., Esplin, T. L., & Loutrel, N. P. 2016, ApJ, 827, 52
Manara, C. F., Testi, L., Natta, A., et al. 2014, A&A, 568, A18
Marois, C., Lafrenière, D., Doyon, R., Macintosh, B., & Nadeau, D. 2006, ApJ, 641, 556
Martin, D. C., Fanson, J., Schiminovich, D., et al. 2005, ApJL, 619, L1
Muley, D., Fung, J., & van der Marel, N. 2019, ApJL, 879, L2
Neugebauer, G., Habing, H. J., van Duinen, R., et al. 1984, ApJL, 278, L1
Neugebauer, G., Habing, H. J., van Duinen, R., et al. 2019, IRAS Point Source Catalog v2.1 (PSC), IPAC, doi:10.26131/IRSA4
O'Meara, J. 2020, KODIAQ Data Release 3, IPAC, doi:10.26135/KOA1
Ortiz-León, G. N., Loinard, L., Dzib, S. A., et al. 2018, ApJ, 865, 73
Owen, J. E., Clarke, C. J., & Ercolano, B. 2012, MNRAS, 422, 1880
Ruane, G., Ngo, H., Mawet, D., et al. 2019, AJ, 157, 118
Skrutskie, M. F., Cutri, R. M., Stiening, R., et al. 2006, AJ, 131, 1163
Skrutskie, M. F., Cutri, R. M., Stiening, R., et al. 2019, 2MASS All-Sky Point Source Catalog, IPAC, doi:10.26131/IRSA2
Soummer, R., Pueyo, L., & Larkin, J. 2012, ApJL, 755, L28
Uyama, T., Hashimoto, J., Muto, T., et al. 2018, AJ, 156, 63
van der Marel, N., Verhaar, B. W., van Terwisga, S., et al. 2016, A&A, 592, A126
Wang, J. J., Ruffio, J.-B., De Rosa, R. J., et al. 2015, pyKLIP: PSF Subtractionfor Exoplanets and Disks, Astrophysics Source Code Library, ascl:1506.001
Wright, E. L., Eisenhardt, P. R. M., Mainzer, A. K., et al. 2010, AJ, 140, 1868
Wright, E. L., Eisenhardt, P. R. M., Mainzer, A. K., et al. 2019, AllWISE Source Catalog, IPAC, doi:10.26131/IRSA1